Fizika Nizkikh Temperatur, 2009, v. 35, No. 6, p. 560–570

Flux pinning and vortex dynamics in MgB_2 doped with TiO_2 and SiC inclusions

V.G. Prokhorov and G.G. Kaminsky

Institute of Metal Physics, National Academy of Sciences of Ukraine, Kiev 03142, Ukraine
E-mail: pvg@imp.kiev.ua

V.L. Svetchnikov

National Center for HREM, TU Delft, 2628AL, The Netherlands

J.S. Park, T.W. Eom, and Y.P. Lee

Quantum Photonic Science Research Center and Department of Physics, Hanyang University, Seoul 133-791, Korea

J.-H. Kang

Department of Nano and Electronics Physics, Kookmin University, Seoul 136-702, Korea

V.A. Khokhlov

Donetsk Institute for Physics and Technology, NASU, Donetsk 83114, Ukraine

P. Mikheenko

Department of Material Science and Metallurgy, University of Cambridge, Cambridge, CB2 3QZ, United Kingdom

Received January 22, 2009, revised February 13, 2009

The mixed-state superconducting properties of bulk MgB_2 + 2 at.% TiO_2 and + 8 at.% SiC, prepared by the *in situ* solid state reaction, have been investigated. The analysis on the mixed-state parameters, such as the upper critical field, the coherence length and the Ginzburg–Landau parameter, proves that the MgB_2 + + 2 at.% TiO_2 is a high-κ type-II superconductor in the dirty limit while the MgB_2 + 8 at.% SiC corresponds to that in the moderately clean limit. It was shown that the anisotropic grain-boundary pinning is realized in the fine-grained doped MgB_2 polycrystals rather than the electron scattering one. The field-cooled temperature dependences of magnetic moment exhibit a transition of the samples to the paramagnetic state at certain applied magnetic fields, which is treated as manifestation of the paramagnetic Meissner effect. The experimental results are discussed on the base of modern theoretical approaches.

PACS: 74.70.Ad Metals; alloys and binary compounds (including A15, MgB_2, etc.);
74.25.Qt Vortex lattices, flux pinning, flux creep;
74.25.Sv Critical currents.

Keywords: pinning, vortex dynamic.

1. Introduction

The superconducting magnesium diboride (MgB_2), with a transition temperature $T_c \simeq 39$ K [1], has emerged to be a promising material for high-magnetic-field applications in a temperature range of liquid hydrogen. The existence of two conduction bands and two superconducting gaps [2], due to the interband and intraband scattering, can lead to a remarkable enhancement in the upper critical field H_{c2} [3]. On the other hand, the critical current density J_c of the bulk MgB_2, prepared by the traditional method, is significantly low compared to the conventional low-T_c superconductors, owing to a poor electrical connection between grains and a lack of flux

pinning centers in the material. It was shown recently that the essential factors for J_c in superconducting MgB_2 are the connectivity and the flux pinning by the grain boundaries [4,5]. For example, a detectable increase in the critical current is observed for the finely crystalline MgB_2 films, prepared by different methods [6,7]. Another way to improve J_c is the introduction (or the doping) of nanosize non-superconducting inclusions in the bulk MgB_2 , including TiO_2 and SiC, which play a role of additional effective pinning centers [8–14].

In real (non-ideal) superconductors, J_c is controlled by the pinning force density, $F_p = -J_c \times B$, where B is magnetic induction, which blocks the vortex motion under the action of the Lorenz force. The F_p value is provided by the pinning mechanism of an individual vortex at the microstructural imperfections (at low magnetic fields) [15] and by the elasticity of flux-line lattice with increasing B significantly [16,17]. The main difficulty in analyzing the flux pinning mechanism and disappearance of the non-dissipative current state in polycrystalline bulk superconductors is connected with the complex microstructure and the chemical inhomogeneity, such as the grain boundaries (GBs), the second-phase inclusions, the intergranular porosity, the screw and the edge dislocations, and so on. All these defects can play a role of the pinning centers with different mechanisms of the vortex-defect interaction. Therefore, the elucidation of flux pinning mechanism in the bulk MgB_2 doped with TiO_2 or SiC should be based on careful study of the microstructure, and analysis of the magnetic field and the temperature dependences of pinning force density. It was shown recently that the Ti-doped MgB_2 manifests a significantly improved J_c due to the greatly refined MgB_2 grains, the formation of a thin TiB_2 layer at the GBs, and the presence of MgO nanoparticles [12,18,19]. On the other hand, the predominant mechanism of flux pinning for this compound remains unclear.

Another peculiarity of the dynamic mixed state of non-ideal superconductors is related to the «paramagnetic Meissner effect» (PME) or «Wohlleben effect», which was observed recently in MgB_2 [20]. In this case the temperature dependence of the magnetic moment (or the magnetic susceptibility) reveals a paramagnetic signal at $T \le T_c$ (instead of a diamagnetic one), when the sample was cooled down in an external magnetic field (the field-cooling regime) [21–24]. The observed paramagnetic response is explained by the formation of a system of multiply connected Josephson junctions (for different *s*- and *d*-wave pairing mechanism) [25–27], which is typical for granular superconductors, or by the non-uniform redistribution of the Abrikosov vortices in the sample upon the heterogenous superconducting transition in an applied magnetic field [28,29].

In this paper, we present the experimental results for the bulk MgB_2 doped with TiO_2 and SiC inclusions. The predominant mechanism of flux pinning and the observed evidence for the PME are discussed in detail.

2. Experimental techniques

The samples were prepared by the *in-situ* solid state reaction, which was described in detail elsewhere [4]. Mechanically alloyed MgB_2 + 2 at.% TiO_2 (MBTO) and MgB_2 + 8 at.% SiC (MBSC) powders were used for the sintering. The average grain size of the nanoparticles was about 30 and 40 nm, for TiO_2 and SiC, respectively. The high-resolution transmission-electron-microscopy (TEM) and the electron-diffraction (ED) studies were carried out by using a Philips CM300UT-FEG microscope with a field emission gun operated at 300 kV. The resolution of microscope was around 0.12 nm. All the microstructural measurements were performed at room temperature. The field-cooled (FC) and the zero-field-cooled (ZFC) temperature dependences of magnetic moment, and the hysteresis loops [$M(H)$] were measured in an applied magnetic field along a sample axis, which was 3–4 times longer than the shorter ones, using a Quantum Design SQUID magnetometer in a temperature range of 2–40 K. The J_c was estimated from the $M(H)$ curves using the extended Bean model [4,14].

3. Microstructures

Figure 1,*a* shows the TEM image for MBTO, manifesting the presence of two regions with different microstructures. The top part (*A*) corresponds to the coarse-grained polycrystal with an average grain size of 50–70 nm, while the bottom one (*B*) exhibits the relatively fine-grained microstructure (the grain size is smaller to be 10 nm). The ED pattern of the sample (see Fig. 1,*b*) reveals that the large- and the small-size grains have the same hexagonal crystal lattice, which is typical for the MgB_2 phase. The moire fringes are also revealed on the TEM images of certain grains (black arrows in Fig. 1,*a*), manifesting presence of the TiB_2 phase, which is isostructural to MgB_2 but has slightly different crystal lattice parameters. a = = 0.3086 and 0.303 nm, and c = 0.3523 and 0.323 nm for MgB_2 and TiB_2, respectively [12]. It is confirmed by the local ED pattern taken from the «moire» grain (see Fig. 1,*c*), which shows a slight splitting of the Bragg spots along the $(001)^*$ direction. In addition, Fig. 1,*a* exhibits the well-defined rectangular inclusions (white arrows), which have a cubic crystal lattice (see the corresponding local ED pattern in Fig. 1,*d*), and are identified as the MgO phase. The average size of these inclusions is about 50 nm. Therefore, the MBTO sample has combined microstructures composed of the small- and the large-size MgB_2 grains, which can be separated by thin TiB_2 inter-

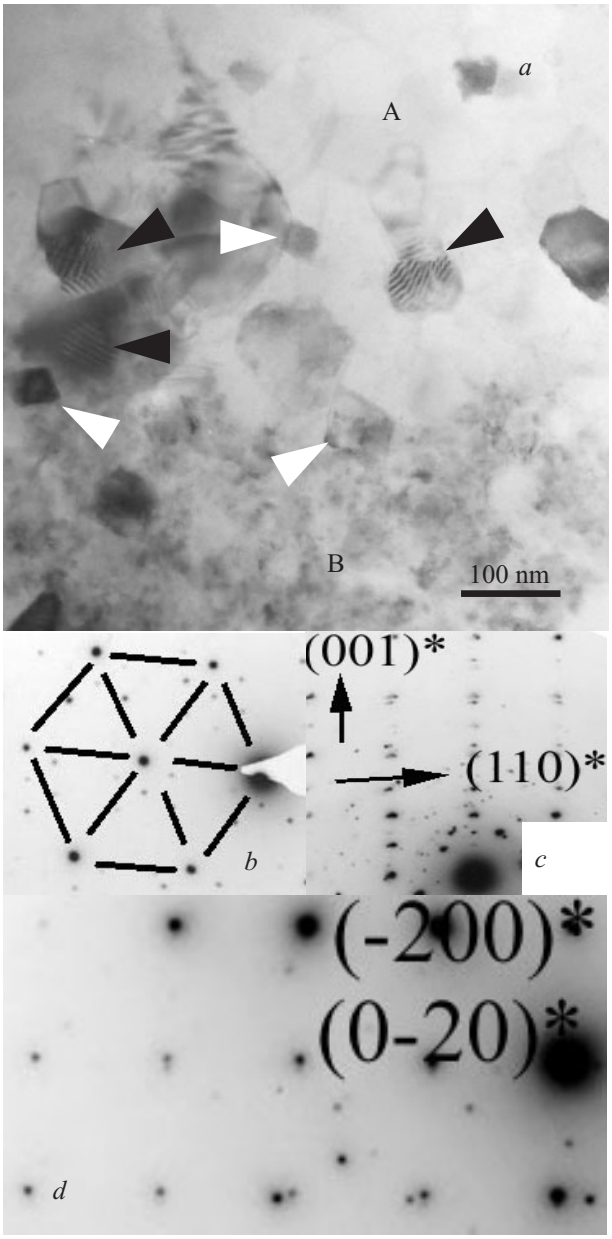

Fig. 1. High-resolution TEM image for MBTO. *A* and *B* indicate the regions of coarse- and fine-grained microstructures, respectively. Black arrows show the moire fringes for stacked grains. White arrows indicate the MgO inclusions (*a*). [0001]-zone-axis selected area ED pattern for the MgB_2 grain (the reflexes are shown) (*b*). [2-1-10]-zone-axis selected area ED pattern for stacked MgB_2 and TiB_2 grains [the (001) reflexes are shown] (*c*). [001]-zone-axis selected area ED pattern for the MgO inclusion (*d*).

layers along the *c* axis, and the MgO inclusions. The obtained results are very close to microstructural data for MgB_2 doped by a pure Ti precipitations [12,18,19].

Figure 2 shows the TEM image for MBSC, indicating that the sintered sample has also a multi-phase polycrystalline microstructure with an average grain size near 200 nm. The ED pattern (see inset (*a*)) reveals that these

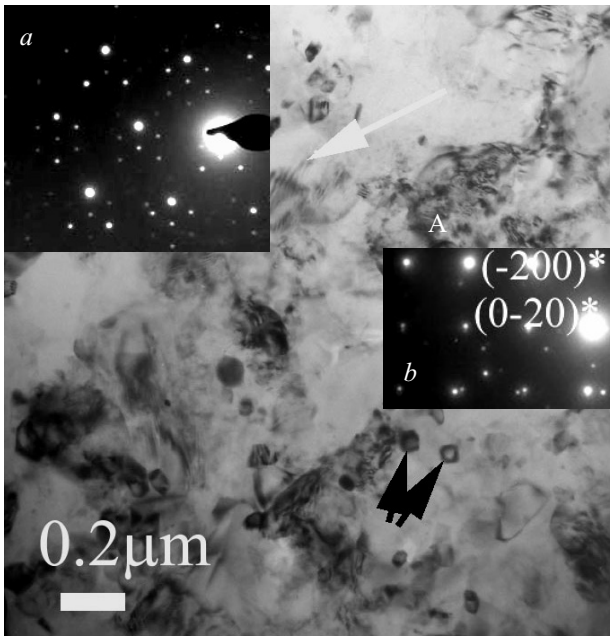

Fig. 2. High-resolution TEM image for MBSC. White arrow indicates the moire fringes for the lattice strain or the presence of an additional phase, which is isostructural to MgB_2. Black arrows mean the MgO inclusions. Inset (*a*) shows the [0001]-zone-axis selected area ED pattern for the MgB_2 grain (the reflexes are shown). Inset (*b*) is the [001]-zone-axis selected area ED pattern for the MgO inclusion.

grains have a hexagonal crystal lattice, which is typical for the MgB_2 phase. The moire fringes, similar to MBTO, are also revealed on the TEM images of certain grains (denoted by white arrow). Such a type of TEM contrast can be treated as accumulation of the lattice strain inside grains or presence of an additional phase, which is isostructural to MgB_2. Most probably this phase corresponds to $MgB_{2-y}C_y$ and is formed by the partial substitution of carbon for boron. The black arrows indicate the well-defined rectangular inclusions, which have a cubic crystal lattice (see the corresponding local ED pattern in the inset (*b*)), and is identified as the MgO phase. The average size of these inclusions is about 50 nm. At the same time, the sample has regions in a subgrain ($\leq$ 10 nm) phase (indicated by *A*), whose chemical composition is undefined.

Therefore, the principal difference between MBTO and MBSC samples is connected with different average grain sizes of the basic MgB_2 phase: 50–70 and 200 nm, respectively.

4. Experimental results

Figure 3 presents the ZFC (*a*) and the FC (*b*) temperature dependences of the magnetic moment, $M(T)$, for MBTO at different applied magnetic fields. It is seen that the ZFC $M(T)$ curves demonstrate the diamagnetic be-

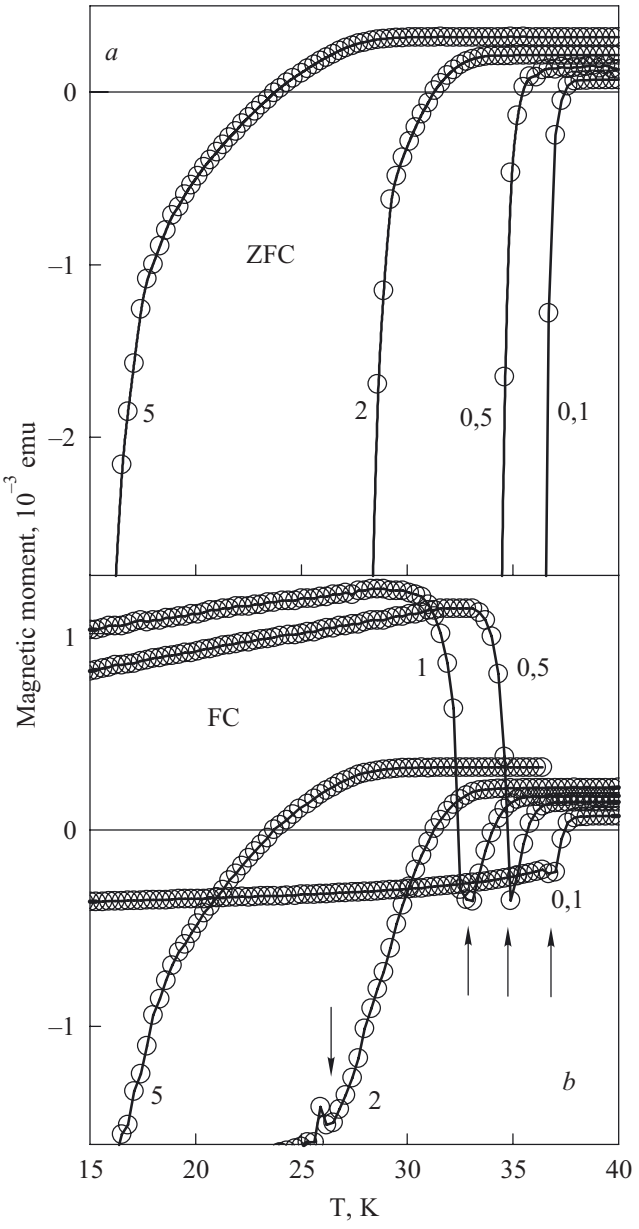

Fig. 3. ZFC (*a*) and FC (*b*) magnetic moment curves for MBTO (numbers are the values of applied magnetic field in T). Arrows in (*b*) indicate the para-diamagnetic transition. Lines are only guides to the eyes.

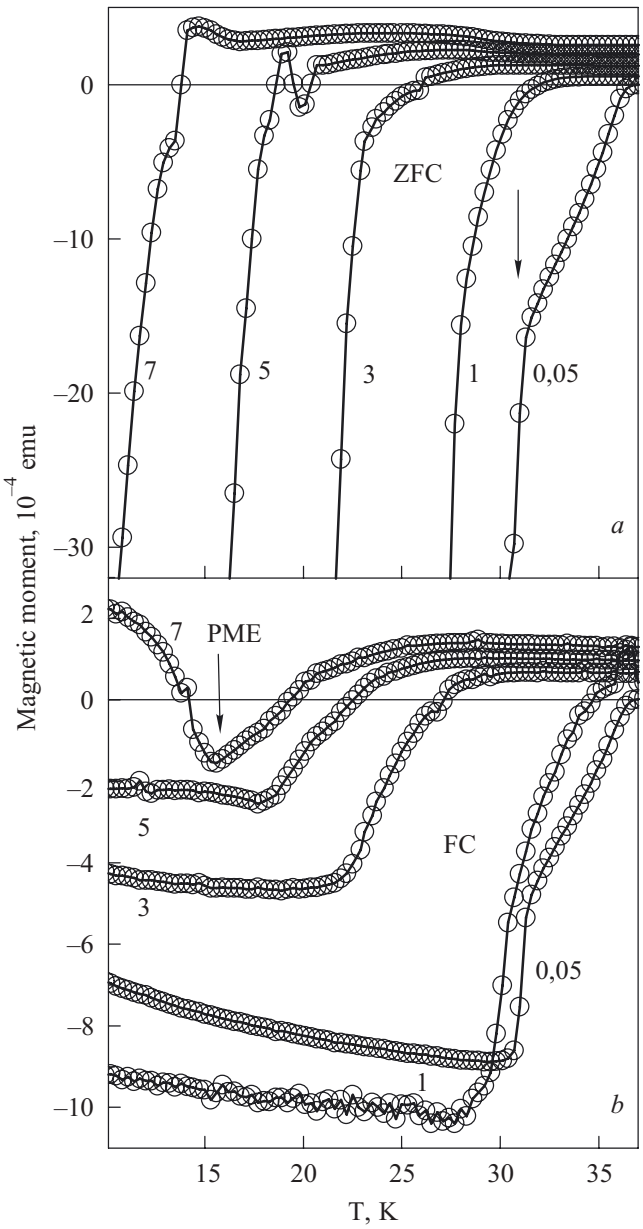

Fig. 4. ZFC (*a*) and FC (*b*) magnetic moment curves for MBSC (numbers are the values of an applied magnetic field in T). Arrow in (*b*) indicates the appearence of PME. Lines are only guides to the eyes.

havior at $T \le T_c$, which is typical for a common superconductor. In contrast to that, the FC $M(T)$ dependencies manifest the transition of the sample in a paramagnetic state at certain temperatures (indicated by arrows), which are significantly below T_c. As stated above, the similar phenomenon have already been observed in the conventional and high-T_c superconductors, and was called by the PME [24].

Figure 4 displays the same $M(T)$ dependencies for MBSC. The sharp change in the ZFC $M(T)$ slop (indicated by arrow) at the lowest external magnetic field (H = = 50 mT) is connected probably with the presence of the carbon reach magnesium diboride phase. The FC $M(T)$ dependencies also generally manifest the diamagnetic behavior, excepting the magnetic field of 7 T. In this case the paramagnetic response occurs at $T \le 15$ K.

Figures 5,*a* and 6,*a* show selected hysteresis loops taken at different temperatures for MBTO and MBSC, respectively. The magnetic moment jumps (or oscillations) are observed in the low-field range with decreasing temperature $T \le 15$ K for MBTO while ones are absent up to $T \le 5$ K for MBSC. This phenomenon is governed by the flux-jump instability of critical state in type-II supercon-

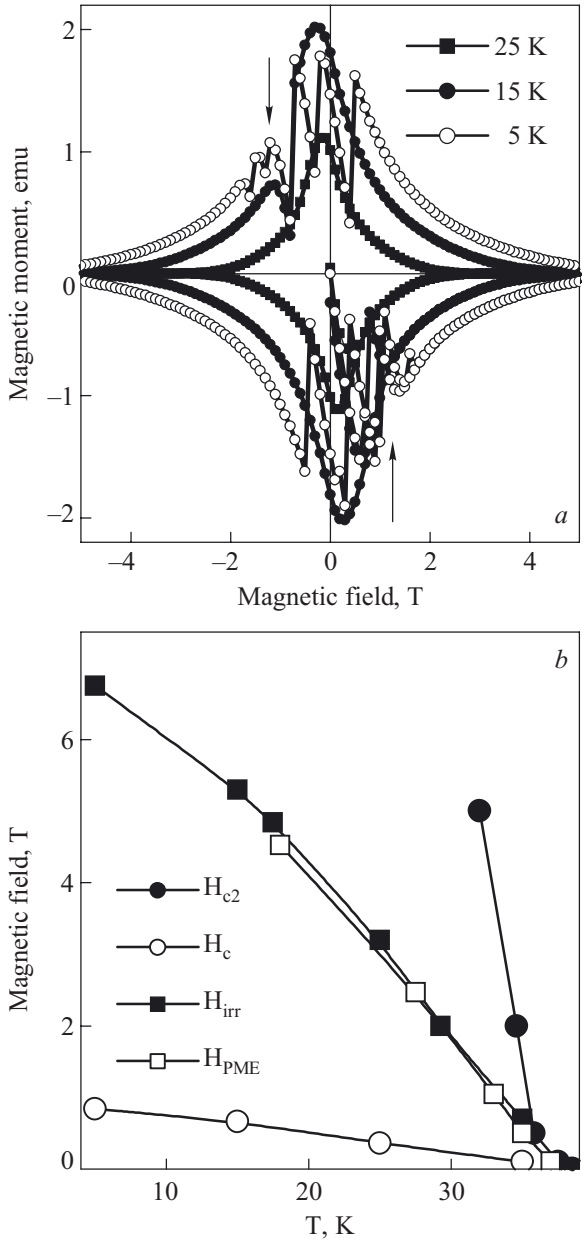

Fig. 5. Hysteresis loops for MBTO at 5, 15 and 25 K. Arrows indicate the flux jumps (*a*). Temperature phase diagrams for the upper critical field H_{c2}, the thermodynamic critical field H_c, the irreversibility field H_{irr}, and the paramagnetic Meissner effect H_{PME}. Lines are only guides to the eyes (*b*).

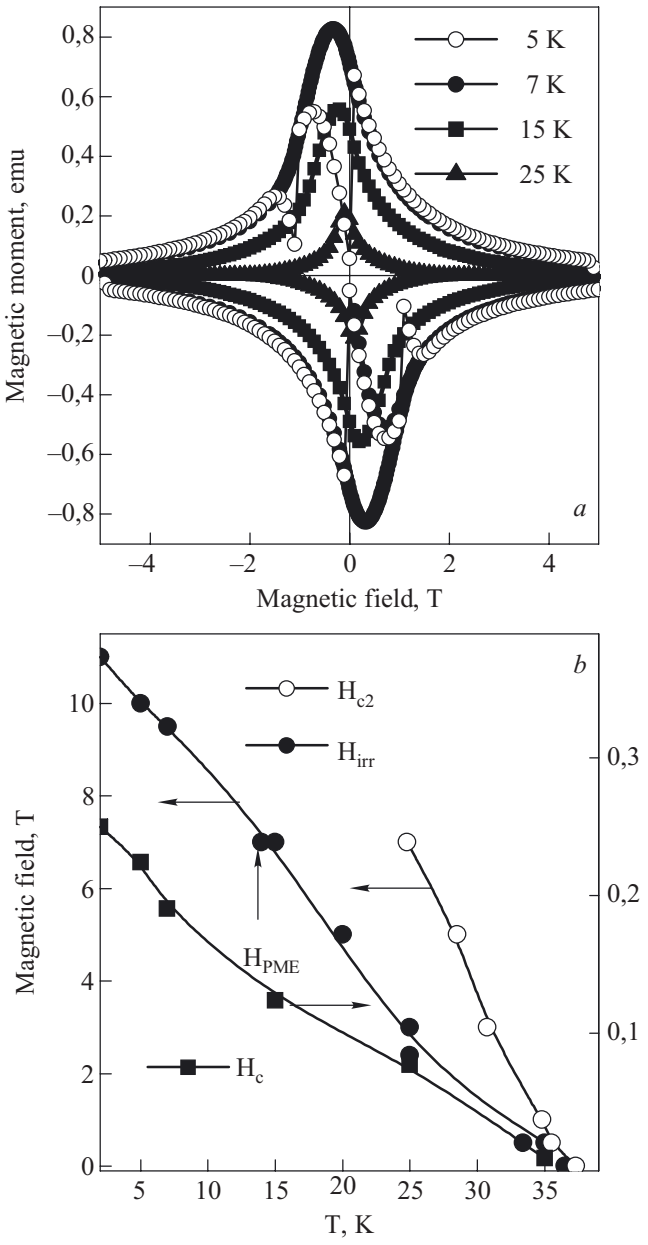

Fig. 6. Hysteresis loops for MBSC at different temperatures (*a*). Temperature phase diagrams for the upper critical field H_{c2}, the thermodynamic critical field H_c, and the irreversibility line H_{irr}. Arrow indicates the point for PME H_{PME}. Lines are only guides to the eyes (*b*).

ductors, and determined by the strong pinning and the thermomagnetic properties of materials [30,31].

Analysis of the experimental data allows us to estimate some critical parameters of the sample, which are summarized in Figs. 5,*b* and 6,*b*. The upper critical magnetic field H_{c2} was determined at a point where the ZFC magnetic moment starts to be deviated from the normal-state linear background. The linear $H_{c2}(T)$ approximation was used for estimation of the upper critical field at $T = 0$, as a most preferable for the two-gap disordered superconductors [32]. More mixed-state parameters can be calculated from London theory and some Ginzburg–Landau relations. The magnetic penetration depth, λ, was obtained from $\partial M / \partial \ln H = \varphi_0 / (8\pi\lambda^2)$, where $\varphi_0 = 2.07 \cdot 10^{-15}$ T·m^2 is the magnetic flux. The high-field reversible $M(H)$ branches were used for the analysis. The reversible magnetic moment is either calculated from the high-field irreversible branches in increasing (M_+) and decreasing (M_-) fields in the fully penetrated state, $(M_+ + M_-)/2$ or directly measured [33]. The coherence

Table 1. The mixed-state superconducting properties of the bulk MgB_2 + 2 at.% TiO_2 and + 8 at.% SiC.

Samples	Upper critical field $H_{c2}(0)$, T	Thermodynamic critical field, $H_c(0)$, T	First critical field $H_{c1}(0)$, mT	Magnetic penetration depth, $\lambda(0)$, nm	Coherence length $\xi(0)$, nm	Ginzburg–Landau parameter, $\kappa(0)$
MBTO	35	0.84	70	90	3.07	29.1
MBSC	23.8	0.25	11.3	250	3.7	68

length was estimated from $\xi(T) = [\varphi_0 / 2\pi H_{c2}(T)]^{1/2}$ and the Ginzburg–Landau parameter as $\kappa(T) = \lambda(T) / \xi(T)$. Because $H_{c2}(T) = \sqrt{2}\ \kappa H_c(T)$, temperature dependence of the thermodynamic critical field H_c can be estimated, as well. The first critical field was obtained from expression $H_{c1} = [\varphi_0 / 4\pi\lambda^2(0)](\ln\kappa + 0.08)$.

For many practical superconductors, including the MgB_2 compound, the critical current can be treated as zero at the irreversibility magnetic field H_{irr}, which is lower than H_{c2} and manifests the transform of $M(H)$ on a reversible branch. Because this process is accompanied by the pinning suppression, just H_{irr} is used, as a rule, for analysis of the pinning force density versus a reduced magnetic field, $b = H / H_{irr}$. The H_{irr} value was determined by taking the splitting point between ZFC and FC $M(T)$ curves and by extrapolating the negative and the positive $M(H)$ branches to the reversible point of magnetic field. The calculated mixed-state parameters are summarized in the Table 1. It should be noted that the obtained results are almost coincident with the published ones for the similar bulk materials or films [10,34,35].

Figures 7,*a* and 8,*a* show the $J_c(H)$ curves at different temperatures obtained from the hysteresis magnetization loops for MBTO and MBSC, respectively. The critical current density was calculated, based on the extended Bean model [4,14], using $J_c(H) = [(M_+ - M_-) / V] \times$ $\times 2 / [d(1 - d / 3w)]$, where $(M_+ - M_-)$ is the width of the hysteresis loop, V is the sample volume, d and w $(d \le w)$ are the dimensions of the sample perpendicular to the applied field.

Figures 7,*b* and 8,*b* display the pinning force density versus a reduced magnetic field, $b = H / H_{irr}$, measured at different temperatures for MBTO and MBSC, respectively. As a rule the field dependence of F_p for type-II superconductors follows a scaling law of $F_p \sim b^p(1-b)^q$ with the maximum at $b_{peak} = p / (p + q)$, which is determined by the sample microstructure and the pinning mechanism [36]. At the same time, Fig. 7,*b* shows that for MBTO the $F_p(b)$ dependence trends to have a double-peak shape with decreasing temperature (indicated by arrows). Such a type of $F_p(b)$ have already been observed in thick MgB_2 films and was explained by two pinning mechanisms at point and planar defects [37]. It was shown recently, that the MgB_2 doped with SiC demonstrates the $F_p(b) \simeq Ab^{0.5}(1-b)^2$ behavior in whole temperature range, where A is a certain numerical factor [4].

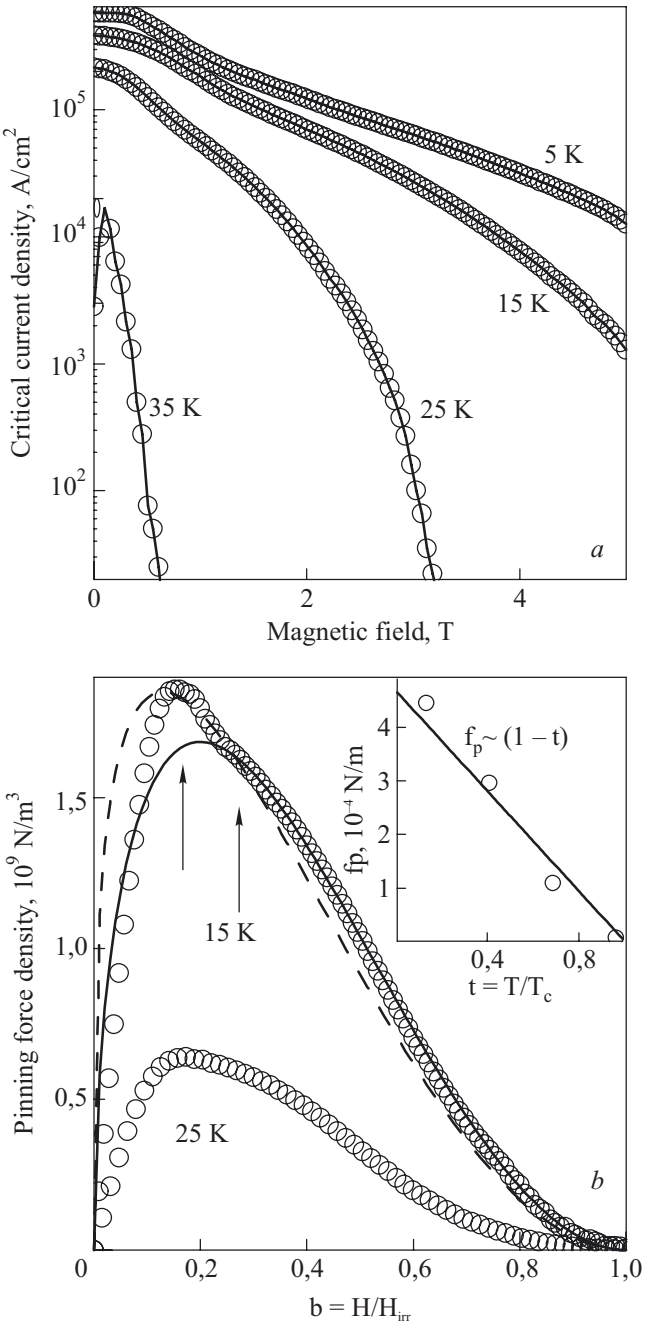

Fig. 7. Magnetic field dependence of the critical current density for MBTO at different temperatures. Lines are only guides to the eyes (*a*). Reduced magnetic field dependence of the pinning force density at 15 and 25 K. Arrows point out the double-peak behavior of $F_p(b)$. Solid and dashed lines are the fitting curves, discussed in text. Inset shows the temperature dependence of the elementary pinning force, $f_p = F_p / N_\upsilon$ where N_υ is the vortex numder (*b*).

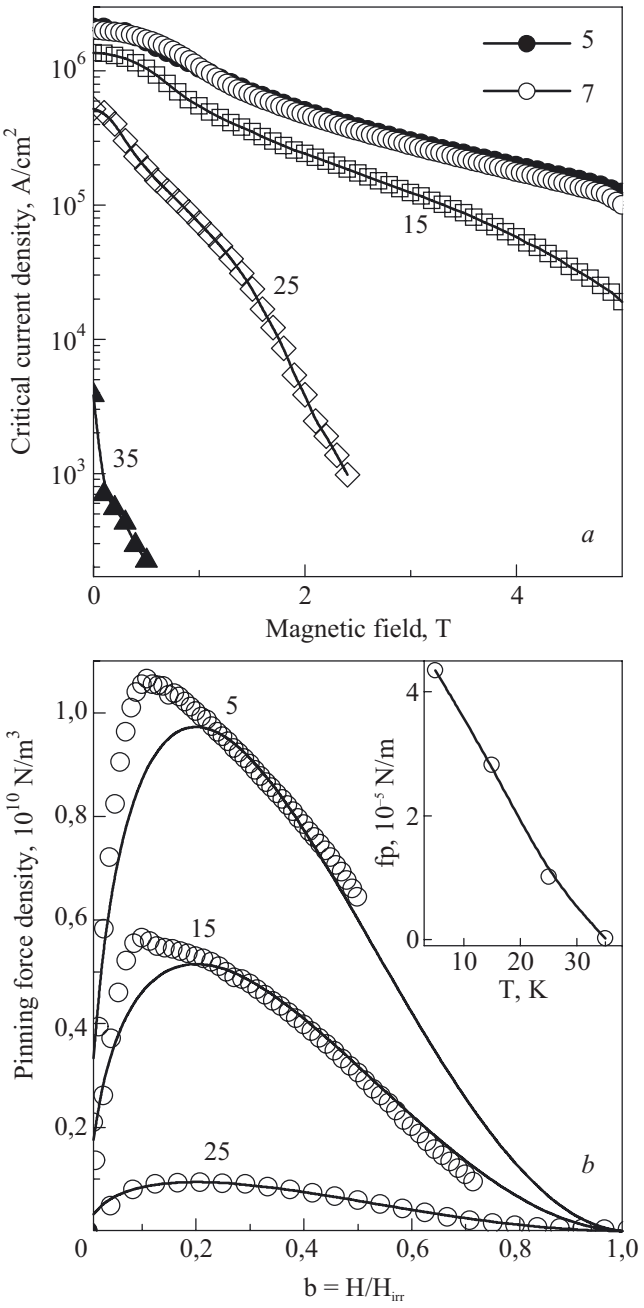

Fig. 8. Magnetic field dependence of the critical current density for MBSC at different temperatures (indicated by numbers). Lines are only guides to the eyes (*a*). Reduced magnetic field dependence of the pinning force density at 5, 15 and 25 K. Solid lines are the fitting curves, discussed in text. Inset shows the temperature dependence of the elementary pinning force, $f_p = F_p / N_\upsilon$, where N_υ is the vortex number (*b*).

The solid lines in Fig. 8,*b* are the same curves with $A = 3.3 \cdot 10^9$, $1.8 \cdot 10^{10}$ and $3.4 \cdot 10^{10}$ N / m^3 for $T = 25$, 15 and 5 K, respectively. It is seen that the experimental curve are excellently coincident with the theoretical one at $T = 25$ K, and significantly deviated from its (particularly in the low-field range) at $T = 15$ and 5 K. One can conclude that the flux pinning mechanism could be changed with decreasing temperature.

5. Discussions

Analysis of the mixed-state parameters, such as the upper critical field, the coherence length and the Ginzburg–Landau parameter, allows us to conclude that the polycrystalline MBTO is a high-κ type-II superconductor in the dirty limit, in contrast to the single-crystalline MgB_2, manifesting the properties typical for a low-κ superconductor in the clean limit [14]. The threshold between moderately clean and moderately dirty limits for MgB_2 is given by $\xi_0 = l$, where ξ_0 is the coherence length resulted from the microscopic theory and l is the electron mean free path, corresponding to $H_{c2} \simeq 27$ T [3], which is smaller than the upper critical field in the case of MBTO. At the same time the analysis of the mixed-state parameters allows us to conclude that the polycrystalline MBSC belongs to a high-κ type-II superconductor in the moderately clean limit, because the $H_{c2}(0) \simeq 23.8$ T is slightly smaller than the threshold value.

The following peculiarities of mixed state, which are observed in MBTO and MBSC, must be discussed in detail. There are the predominant mechanism of flux pinning and the origin of PME.

Flux pinning and vortex dynamics

The pinning force density at low magnetic field (when the vortex number, N_υ, is smaller than the number of pinning centers) can be expressed by a direct summation on vortices, because only the pinning interactions have be summarized: $F_p = f_p N_\upsilon$, where f_p is the elementary pinning force. Taking into account that $N_\upsilon \simeq H / \varphi_0$, one can write $f_p \simeq \varphi_0 dF_p / dH|_{H \to 0}$ and use this expression for the estimation of f_p value from the experimental $F_p(H)$ curves. The obtained results for the elementary pinning force are represented by the insets in Figs. 7,*b* and 8,*b* for MBTO and MBSC, respectively. It is seen that f_p decrease with increasing temperature for both the samples and described by an empirical expression $f_p \simeq \simeq f_p(0)(1-t)$, where $f_p(0) = 4.7 \cdot 10^{-4}$ and $5.0 \cdot 10^{-5}$ N/m for MBTO and MBSC, respectively, is the elementary pinning force at $T = 0$ and $t = T / T_c$. The observed linear temperature dependence of f_p will be discussed later.

The vast majority experimental results evidence that the grain boundaries (GBs) are dominant pinning centers in the MgB_2 superconductors [4,5,38,39]. The most discussed mechanism for the GB pinning is based on the possible decrease of a coherence length near GB, due to the electron scattering [40,41]. The simplified expression for the electron scattering GB elementary pinning force can be written as [41] $f_p(0) = 0.115\ [B_c^2 \xi(0) / \mu_0]$, where μ_0 is a magnetic constant. The maximum values of $f_p(0)$,

which were calculated within the framework of this model using the obtained mixed-state superconducting parameters, turn out to be $1.98 \cdot 10^{-4}$ and $2.1 \cdot 10^{-5}$ N/m for MBTO [$H_c(0) = 0.84$ T and $\xi(0) = 3.07$ nm] and MBSC [$H_c(0) = 0.25$ T and $\xi(0) = 3.7$ nm], respectively, that are twice smaller than the experimental values. This disagreement testifies that the electron scattering GB pinning probably can not be realized perfectly in the such type of superconductors. It is believable that the electron scattering GB pinning is greatly suppressed with decreasing the grain size, owing to the complete averaging of the electron mean free path through the whole grain volume and disappearance of the coherence length gradient near GB [40–42]. It is more reasonable to suggest that the vortex pinning in a fine-grained microstructure is governed by the significant anisotropy of the mixed-state superconducting parameters and the random orientation of the adjacent grains. [43] The preference in this case is the anisotropic GB pinning, which is governed by a significant change in the coherence length (or the upper critical field) at the transition of vortex through the boundary between adjacent grains. It is known that the coherence length is different in the *ab* plane and in the *c* direction for the MgB_2 single crystal: $\xi^{ab}(0) = \gamma \xi^{c}(0)$ where γ is the anisotropy coefficient [33]. Therefore, the energy difference for formation of a vortex in the *c* and the *a-b* oriented grains is equal to $\pi B_c^2 \Delta\xi^2(0)/2\mu_0$, where $\Delta\xi(0) = \xi^{ab}(0) - \xi^{c}(0)$. The vortex feels the spatial variation of the potential during its displacement by about the coherence length, and the elementary pinning force can be given by

$$f_p(0) \simeq p(B_c^2/2\mu_0)[\Delta\xi^2(0)/\xi(0)] =$$

$$= p(2B_c^2/\mu_0)[(\gamma-1)/(\gamma+1)]\xi(0),$$

where $p \simeq 0.22$ is the probability for the neighboring grains to be most randomly oriented and $\xi(0)$ is the experimental (average) coherence length. By using again the obtained mixed-state parameters and $\gamma \simeq 4$ [3], it was found that $f_p(0) \simeq 4.55 \cdot 10^{-4}$ and $4.9 \cdot 10^{-5}$ N/m for MBTO and MBSC, respectively, which are coincident well with the experiment. Moreover, the linear temperature dependence of the elementary pinning force, represented by the insets in Figs. 7,*b* and 8,*b*, is an analog to that for the anisotropy parameter [39]. Therefore, one can conclude that the anisotropic GB pinning is realized in the MBTO and MBSC polycrystals rather than the electron scattering one.

Now let us consider the double-peak behavior of $F_p(b)$ in MBTO. The microstructural analysis reveals that the MgO nanoparticles and the isostructural TiB_2 phase (see Fig. 1,*a*) have a low concentration in this sample and cannot play an essential role in the pinning process. Therefore, the double-peak shape of the $F_p(b)$, represented by Fig. 7,*b*, is not explained by the action of two different pinning mechanisms [37], but is rather governed by presence of the regions with different sizes of the grains ((*A*) and (*B*) areas in Fig. 1,*a*). The decrease of grain size leads to significant suppression of both the electron scattering and the anisotropic GB pinning. Therefore, the fine- and the large-grained regions should demonstrate different pinning interactions. Both the field location and the height of the peak of $F_p(b)$ are very sensitive to the elementary pinning force value. For example, the formation of weak widely spaced pinning centers results in a small peak on $F_p(b)$ at a high *b* while the strong closely spaced pins form a large peak at a low *b* [44]. Figure 7,*b* shows that the experimental $F_p(b)$ dependance can be approximated by two fitting curves $Ab^{0.5}(1-b)^2$ (solid line) and $Bb^{0.3}(1-b)^2$ (dashed line), where $A = 6 \cdot 10^9$ and $B = 4.5 \cdot 10^9$ N / m^3 are the fitting parameters. It is concluded that these empirical expressions describe the flux pinning in the sample regions with different microstructures.

The similar reason explains the deviation of $F_p(b)$ from an empirical function $b^{0.5}(1-b)^2$ with decreasing temperature for MBSC (see Fig. 8,*b*). Figure 9 shows the same experimental curves for the relative pinning force density with respect to the maximum F_p^{max} value. It is clearly distinguished that the peak position of the $F_p / F_p^{max}(b)$ curve is shifted in the low-field range and its behavior is fitted more exactly by an empirical function of $b^{0.3}(1-b)^2$ at $T \leq 25$ K. Taking into account, that the elementary pinning force increases with decreasing temperature (see inset in Fig. 8,*b*), the observed modification of the $F_p(b)$ shape is quite expectable.

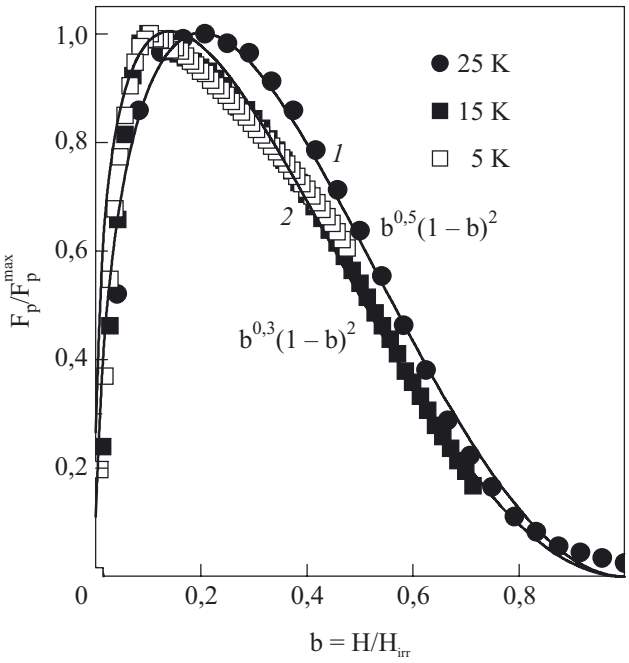

Fig. 9. Magnetic field dependence of the reduced pinning force density for MBSC at different temperatures. Solid lines are the fitting curves, discussed in text.

Paramagnetic meissner effect

Figures 3,*b* and 4,*b* display that the paramagnetic response appears on the FC $M(T)$ dependences within a certain range of applied magnetic field, 0.1 T $\leq H <$ 2 T, for MBTO and at $H \geq$ 7 T for MBSC. Moreover, the transition from paramagnetic to diamagnetic state is occurred by a jump with increasing temperature and its the phase diagram, $H_{PME}(T)$, is exactly coincident with the irreversibility line, $H_{\rm irr}(T)$ (see Figs. 5,*b* and 6,*b*). Therefore, one can conclude that the vortex trapping is a necessary requirement for the PME observation in our case. Such a task has already considered theoretically in the framework of the self-consistent solution of Ginzburg–Landau equations [29] and Bean model [28]. The both approaches predict formation of the inhomogeneous («compressive») vortex state as the superconductor is cooled down in a magnetic field across T_c, which introduces the paramagnetic contribution to the total magnetic moment of sample. The first approach [29] was developed for a long superconducting cylinder in a parallel magnetic field. The model predicts existence of vortices inside the sample in the metastable state that leads to appearance of the PME. The metastable states are introduced in a superconductor by vortex pinning, which is the source of inhomogeneous distribution of the vortices. According to this model the paramagnetic states can exist only within a certain range of magnetic fields and disappear at very low and very large magnetic fields. Moreover, the jump transitions between the paramagnetic and the diamagnetic states are also prognosticated. Therefore, the model demonstrates a good qualitative agreement with the obtained experimental data. However, the more detailed numerical analysis finds out serious contradictions between theory and experiment. For example, the PME, described by this model, is possible only for superconductors larger than a particular size. This size is defined by a dimension parameter: $A = \kappa^{-1}(2\pi R^2 H/\varphi_0)^{1/2}$, where R is the sample radius. According to this, the transition from diamagnetic to paramagnetic state is expected at $A \geq$ 1. For our samples, which have $\pi R^2 = 0.94 \cdot 10^{-6}\,\mathrm{m}^2$, $A \leq 1$ at an applied magnetic fields $H \leq 6.8 \cdot 10^{-4}$ Oe, which is greatly smaller than the magnetic field of earth. Consequently, the theoretical model indicates in our case that the PME should be observed at all employed magnetic fields, which is completely different from the experiment. The second consideration [28] reveals that $M/M_{\rm M} \propto f(a, b/w)$, where M_M is the magnetic moment in the Meissner state, a is the fraction of trapped flux, b is the width of region with the critical current flowing (the region of «flux compression»), and w is the sample diameter. According to this model, the magnetic moment becomes more paramagnetic with increasing both a and flux compression (decreasing b/w). In the case of complete flux trapping (a = = 1) M is always paramagnetic while a pinning-free superconductor ($J_c = 0$) testifies the diamagnetic response only. However, the following complications do not allow us to use this model for the interpretation of experimental results. There are the experimentally nonmeasurable parameters of a and b in the model, the considered sample geometry corresponds to a thin plate or disk in the perpendicular magnetic field, and the employment of the Bean model is for a description on the «compressive» vortex state.

Taking into account all mentioned above, we suggest a following explanation of the origin for PME in the polycrystalline MBTO and MBSC superconductors. The heterogeneous superconducting transition in the external magnetic field occurs with decreasing temperature due to a great anisotropy of the upper critical field, which is typical for the MgB_2 compound [33]. The random grain (or grain group) orientation relative to the external field creates a significant variety of T_c in the different grains, because the $H_{c2}(T)$ behavior is strongly dependent on the crystal lattice axis. Figure 10 displays that the grains (orgrain groups), whose *ab* planes are oriented parallel to H become superconducting first (T_c^{ab}) while the ones

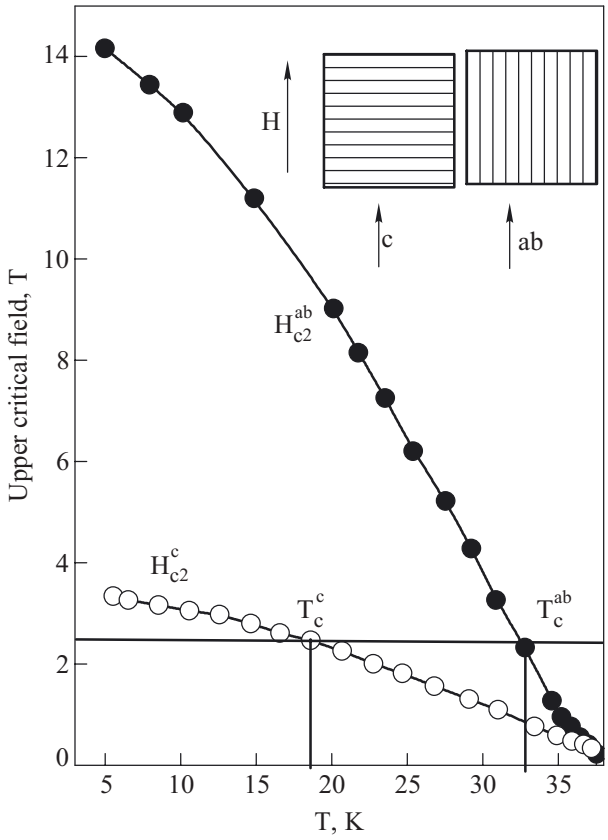

Fig. 10. Temperature dependence of the upper critical field along *ab* and *c* axis of MgB_2 single crystal (Ref. 33). If the sample is cooled down in the external magnetic field (straight line parallel to *T*-axis) the grains, whose *ab* planes are oriented parallel to H become superconducting first T_c^{ab} while the ones with $c||H$ orientation have the lower critical temperature T_c^{c}.

with $c||H$ orientation have the lower critical temperature (T_c^c). Certainly, it is correct only for a case, when the sample is cooled in the external magnetic field. The superconducting grains trend to displace the vortices in the adjacent «bad»-oriented ones. However, this strength is compensated by the GB pinning force and resulted in a creation of the «compressive» vortex state. Because the «compressive» vortex state is characterized by the heterogeneous flux distributing, the critical current flowing must be occurred in such regions. This current has an opposite direction relative to the Meissner one and determines a positive sign of magnetic moment. The total magnetic moment can be expressed as a superposition of two contributions: $M = -M(J_M) + M(J_c)$, where $-M(J_M)$ and $M(J_c)$ are the diamagnetic (Meissner) and the paramagnetic (PME) magnetic moments, respectively. The $M(J_c)$ is directly determined by the pinning force. It is confirmed by the full coincidence between the $H_{\rm PME}(T)$ and the $H_{\rm irr}(T)$ experimental curves. Because the pinning force density demonstrates non-monotonic magnetic field dependence, the $M(J_c)$ contribution will be also decreased at low and high external magnetic fields, leading to disappearance of the PME in these regions. The offered explanation substantially coincides with the outline of the considered model [28]. The fundamental differences consist of the nature of heterogeneous superconducting transition and the origin of the critical Bean state in the separated areas of the sample. Therefore, it is concluded that the paramagnetic Meissner effect in polycrystalline MBTO and MBSC is governed by the significant anisotropy of the superconducting parameters and the microstructural peculiarities rather than the geometry and the size of sample.

Moreover, such a type of flux heterogeneity is confirmed by the unusual behavior of magnetization relaxation. Figure 11 displays the time dependences of reduced magnetic moment at 10 K, which are obtained after cooling down of the samples in an external magnetic field of 1 T followed by the subsequent switching off. The dashed lines are fitting curves corresponding to the interpolation formula suggested by the collective vortex creep theory [45] with a pinning potential height of $U_0 \simeq 25$ and 17.6 meV, for MBTO and MBSC, respectively. The main unexpected peculiarity in the $M(\tau)/M(0)$ behavior is appearance of a large magnetic noise at $\tau \geq 100$ s (indicated by arrow), which can be explained by the intrinsic inhomogeneity of a superconductor [46]. As aforementioned, the mixed-state inhomogeneity in the external magnetic field in our case is governed by the upper critical field anisotropy.

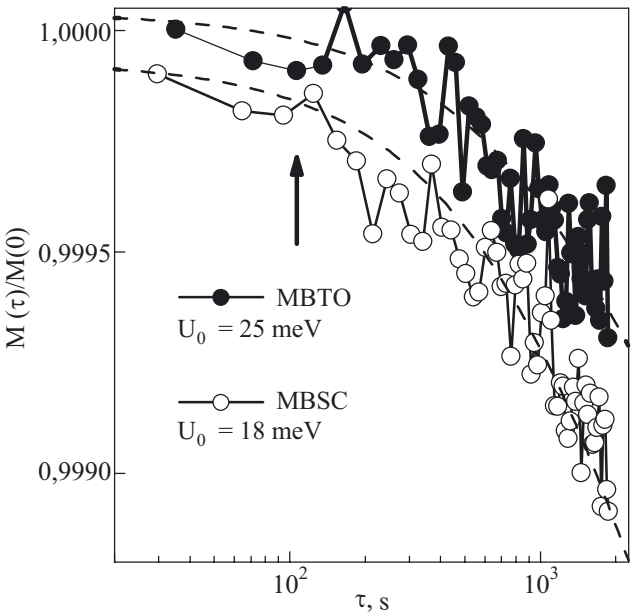

Fig. 11. Time dependence of the magnetic moment at $T = 10$ K in an external magnetic field of 1 T. Solid lines are only guides to the eyes. Arrow indicates the beginning of magnetic noise. Dashed lines are the fitting curves based on the collective creep theory.

6. Conclusions

The mixed-state superconducting properties of the bulk MgB_2 + 2 at.% TiO_2 and + 8 at.% SiC, prepared by the *in-situ* solid state reaction, have been investigated. The high-resolution TEM study reveals that the samples have combined microstructures, consisting of the MgB_2 phase with an average grain size of 50 and 200 nm, for the TiO_2 and the SiC doping, respectively, and the MgO inclusions. The analysis on the mixed-state parameters, such as the upper critical field, the coherence length and the Ginzburg–Landau parameter, proves that the MgB_2 + 2 at.% TiO_2 is a high-κ type-II superconductor in the dirty limit while the MgB_2 + 8 at.% SiC corresponds to that in the moderately clean limit. It was shown that the anisotropic GB pinning is realized in the fine-grained doped MgB_2 polycrystals rather than the electron scattering one. In contrast to the ZFC $M(T)$ curves, which always manifest the diamagnetic response at $T < T_c$, the FC $M(T)$ dependences exhibit the transition of the sample in a paramagnetic state at certain magnetic fields. This phenomenon is treated as an evidence for the paramagnetic Meissner effect. Moreover, the transition from paramagnetic to diamagnetic state occurs by a jump with increasing temperature and the phase diagram, $H_{\rm PME}(T)$, is exactly coincident with the irreversibility line, $H_{\rm irr}(T)$. It was concluded that the observed PME is governed by the significant anisotropy of the superconducting parameters and the microstructural peculiarities rather than the geometry and the size of sample.

Acknowledgments

This work was supported by the KOSEF through the Quantum Photonic Science Research Center, by MEST, and by Research fund of HYU (HYU-2008-000-0000-7783), Korea. V. Svetchnikov is grateful to the financial support by Netherlands Institute for Metal Research.

1. J. Nagamatsu, N. Nakagawa, T. Muranaka, Y. Zenitani, and J. Akimitsu, *Nature* **410**, 63 (2001).
2. H.J. Choi, D. Roundy, H. Sun, M.L. Cohen, and S.G. Louie, *Nature* **418**, 758 (2002).
3. M. Eisterer, *Supercond. Sci. Technol.* **20**, R47 (2007).
4. E. Martínez, P. Mikheenko, M. Martínez-López, A. Millán, A. Bevan, and J.S. Abell, *Phys. Rev.* **B75**, 134515 (2007).
5. T. Matsushita, M. Kiuchi, A. Yamamoto, J. Shimoyama and K. Kishio, *Supercond. Sci. Technol.* **21**, 015008 (2008).
6. H.-J. Kim, W.N. Kang, E.-M. Choi, M.S. Kim, K.H.P. Kim, and S.-I. Lee, *Phys. Rev. Lett.* **87**, 087002 (2001).
7. S.Y. Xu, Qi Li, E. Wertz, Y.F. Hu, A.V. Pogrebnyakov, X.H. Zeng, X.X. Xi, and J.M. Redwing, *Phys. Rev.* **B68**, 224501 (2003).
8. S.X. Dou, S. Soltanian, J. Horvat, X.L. Wang, S.H. Zhou, M. Ionescu, H.K. Liu, P. Munroe, and M. Tomsic, *Appl. Phys. Lett*. **81**, 3419 (2002).
9. Y. Ma, X. Zhang, G. Nishijima, K. Watanabe, S. Awaji, and X. Bai, *Appl. Phys. Lett*. **88**, 072502 (2006).
10. W.K. Yeoh, J. Horvat, J.H. Kim, X. Xu, and S.X. Dou, *Appl. Phys. Lett*. **90**, 122502 (2007).
11. Q.W. Yao, X.L. Wang, J. Horvat, and S.X. Dou, *Physica* **C402,** 38 (2004).
12. Y. Zhao, Y. Feng, T. Machi, C.H. Cheng, D.X. Huang, Y. Fundamoto, N. Koshizuka, and M. Murakami, *Europhys. Lett.* **57**, 437 (2002).
13. A. Xu, Y. Ma, D. Wang, Z. Gao. X. Zhang, and K. Watanabe, *Physica* **C466**, 190 (2007).
14. C. Krutzler, M. Zehetmaier, M. Eisterer, H.W. Weber, N.D. Zhigadlo, and J. Karpinski, *Phys. Rev.* **B75**, 224510 (2007).
15. A.M. Campbell and J.E. Evetts, *Critical Currents in Superconductors*, Taylor and Francis Ltd., London (1972).
16. A.I. Larkin and Yu.N. Ovchinnikov, *Physica* **C126**, 187 (1984).
17. E.H. Brandt, *Phys. Rev.* **B34**, 6514 (1986).
18. Y. Zhao, D.X. Huang, Y. Feng, C.H. Cheng, L. Zhou, Y. Wu, T. Machi, Y. Fundamoto, N. Koshizuka, and M. Murakami, *Appl. Phys. Lett*. **79**, 1154 (2001).
19. Y. Zhao, Y. Feng, C.H. Cheng, T. Machi, N. Koshizuka, and M. Murakami, *Appl. Phys. Lett*. **80**, 1640 (2002).
20. H. Sözeri, L. Dorosinskii, U. Topal, and I. Ercan, *Physica* **C408-410**, **109** (2004).
21. F.T. Dias, P. Pureur, P. Rodrigues, Jr., and X. Obrados, *Physica* **C354**, 219 (2001).
22. A.I. Rykov, S. Tajima, and F.V. Kusmartsev, *Phys. Rev.* **B55**, 8557 (1997).
23. L. Pust, L.E. Wenger, and M.R. Koblischka, *Phys. Rev.* **B58**, 14191 (1998).
24. M.S. Li, *Phys. Rep.* **376**, 133 (2003).
25. M. Sigrist and T.M. Rice, *Rev. Mod. Phys*. **67**, 503 (1995).
26. B.Z. Spivak and S.A. Kivelson, *Phys. Rev.* **B43**, 3740 (1991).
27. A.P. Nielsen, A.B. Cawthorne, P. Barbara, F.C. Wellstood, L.J. Lobb, R.S. Newrock, and M.G. Forrester, *Phys. Rev.* **B62**, 14380 (2000).
28. A.E. Koshelev and A.I. Larkin, *Phys. Rev.* **B52**, 13559 (1995).
29. G.F. Zharkov, *Phys. Rev.* **B63**, 214502 (2001).
30. Y. Kimishima, S. Takami, T. Okuda, M. Uehara, T. Kuramoto, and Y. Sugiyama, *Physica* **C463-465**, 281 (2007).
31. I. Felnera, V.P.S. Awana, M. Mudgel, and H. Kishan, *J. Appl. Phys*. **101**, 09G101 (2007).
32. V. Braccini A. Gurevich, J.E. Giencke, M.C. Jewell, C.B. Eom, D.C. Larbalestier, A. Pogrebnyakov, Y. Cui, B.T. Liu, Y.F. Hu, J.M. Redwing, Q. Li, X.X. Xi, R.K. Singh, R. Gandikota, J. Kim, B. Wilkens, N. Newman, J. Rowell, B. Moeckly, V. Ferrando, C. Tarantini, D. Marré, M. Putti, C. Ferdeghini, R. Vaglio, and E. Haanappel, *Phys. Rev.* **B71**, 012504 (2005).
33. M. Zehetmayer, M. Eisterer, J. Jun, S.M. Kazakov, J. Karpinski, A. Wisniewski, and H.W. Weber, *Phys. Rev.* **B66**, 052505 (2002).
34. G. Serrano, A. Serquisa, S.X. Dou, S. Soltanian, L. Civale, B. Maiorov, T.G. Holesinger, F. Balakirev, and M. Jaime, *J. Appl. Phys*. **103**, 023907 (2008).
35. J. Chen, V. Ferrando, P. Orgiani, A.V. Pogrebnyakov, R.H.T. Wilke, J.B. Betts, C.H. Mielke, J.M. Redwing, X.X. Xi, and Q. Li, *Phys. Rev.* **B74**, 174511 (2006).
36. W.A. Fietz and W.W. Webb, *Phys. Rev.* **178**, 657 (1969).
37. S.G. Jung, W.K. Seong, N.H. Lee, M. Ranot, and W.N. Kang, *J. Korean*. *Phys. Soc.* **53**, 727 (2008).
38. P. Mikheenko, E. Martínez, A. Bevan, J.S. Abell, and J.L. MacManus-Driscoll, *Supercond. Sci. Technol.* **20**, S264 (2007).
39. M. Eisterer, M. Zehetmayer, and H.W. Weber, *Phys. Rev. Lett*. **90**, 247002 (2003).
40. W.E. Yetter, D.A. Thomas, and E.J. Kramer, *Philos. Mag*. **B46**, 523 (1982).
41. G. Zerweck, *J. Low Temp. Phys*. **42**, 1 (1981).
42. V.G. Prokhorov, C.G. Tretyachenko, and G.G. Kaminsky, *Fiz. Nizk. Temp*. **10**, 878 (1984) [*Sov. J. Low Temp. Phys*. **10**, 461 (1984)].
43. V.M. Pan, S.V. Gaponov, G.G. Kaminsky, D.V. Kuzin, V.I. Matsui, V.G. Prokhorov, M.D. Strikovsky, and C.G. Tretiatchenko, *Cryogenics* **29**, 392 (1989).
44. E.J. Kramer, *J. Appl. Phys*. **44**, 1360 (1972).
45. Y. Yeshurn, A.P. Malozemoff, and A. Shaulou, *Rev. Mod. Phys*. **68**, 911 (1996).
46. A. Mumtaz, W. Setyawan, and S.A. Shaheen, *Phys. Rev.* **B65**, 020503 (2001).